Solar Orbiter First Results (Nominal Mission Phase)

Particle monitoring capability of the Solar Orbiter Metis coronagraph through the increasing phase of solar cycle 25

C. Grimani[1,2], V. Andretta[3], E. Antonucci[4], P. Chioetto[5,6], V. Da Deppo[5], M. Fabi[1,2], S. Gissot[7], G. Jerse[8], M. Messerotti[8], G. Naletto[9,5], M. Pancrazzi[4], A. Persici[10,11], C. Plainaki[12], M. Romoli[13,14], F. Sabbatini[1,2], D. Spadaro[15], M. Stangalini[12], D. Telloni[4], L. Teriaca[16], M. Uslenghi[17], M. Villani[1,2], L. Abbo[4], A. Burtovoi[14], F. Frassati[4], F. Landini[4], G. Nicolini[4], G. Russano[3], C. Sasso[3], and R. Susino[4]

[1] DiSPeA, University of Urbino Carlo Bo, Via S. Chiara 27, 61029 Urbino (PU), Italy
e-mail: `catia.grimani@uniurb.it`
[2] INFN, Via Bruno Rossi 1, 50019 Sesto Fiorentino, Florence, Italy
[3] INAF - Astronomical Observatory of Capodimonte, Salita Moiariello 16, 80131 Naples, Italy
[4] INAF - Astrophysical Observatory of Turin, Via Osservatorio 20, 10025 Pino Torinese (TO), Italy
[5] CNR - IFN, Via Trasea 7, 35131, Padova, Italy
[6] CISAS, Centro di Ateneo di Studi e Attività Spaziali "Giuseppe Colombo", via Venezia 15, 35131 Padova, Italy
[7] Solar-Terrestrial Centre of Excellence - SIDC, Royal Observatory of Belgium, Ringlaan -3- Av. Circulaire, 1180 Brussels, Belgium
[8] INAF - Astrophysical Observatory of Trieste, Via Giambattista Tiepolo 11, 34149 Trieste, Italy
[9] Dip. di Fisica e Astronomia "Galileo Galilei", Universitá di Padova, Via G. Marzolo, 8, 35131 Padova, Italy
[10] Politecnico di Milano, Milano, Piazza Leonardo da Vinci 32, 20133 Milano, Italy
[11] European Space Agency, ESAC, Camino Bajo del Castillo s/n, Villafranca del Castillo, 28692 Villanueva de la Cañada, Madrid, Spain
[12] ASI - Italian Space Agency, Via del Politecnico snc, 00133 Rome, Italy
[13] University of Florence, Physics and Astronomy Department, Largo E. Fermi 2, 50125 Florence, Italy
[14] INAF - Arcetri Astrophysical Observatory, Largo Enrico Fermi 5, 50125 Florence, Italy
[15] INAF - Catania Astrophysical Observatory, Via Santa Sofia 78, 95123 Catania, Italy
[16] Max Planck Institute for Solar System Research, Justus-von-Liebig-Weg 3, 37077 Göttingen, Germany
[17] National Institute for Astrophysics, Institute of Space Astrophysics and Cosmic Physics of Milan, Via Alfonso Corti 12, 20133 Milano, Italy

ABSTRACT

Context. Galactic cosmic rays (GCRs) and solar particles with energies greater than tens of MeV penetrate spacecraft and instruments hosted aboard space missions. The Solar Orbiter Metis coronagraph is aimed at observing the solar corona in both visible (VL) and ultraviolet (UV) light. Particle tracks are observed in the Metis images of the corona. An algorithm has been implemented in the Metis processing electronics to detect the VL image pixels crossed by cosmic rays. This algorithm was initially enabled for the VL instrument only, since the process of separating the particle tracks in the UV images has proven to be very challenging.
Aims. We study the impact of the overall bulk of particles of galactic and solar origin on the Metis coronagraph images. We discuss the effects of the increasing solar activity after the Solar Orbiter mission launch on the secondary particle production in the spacecraft.
Methods. We compared Monte Carlo simulations of GCRs crossing or interacting in the Metis VL CMOS sensor to observations gathered in 2020 and 2022. We also evaluated the impact of solar energetic particle events of different intensities on the Metis images.
Results. The study of the role of abundant and rare cosmic rays in firing pixels in the Metis VL images of the corona allows us to estimate the efficiency of the algorithm applied for cosmic-ray track removal from the images and to demonstrate that the instrument performance had remained unchanged during the first two years of the Solar Orbiter operations. The outcome of this work can be used to estimate the Solar Orbiter instrument's deep charging and the order of magnitude for energetic particles crossing the images of Metis and other instruments such as STIX and EUI.

Key words. instrumentation: detectors – solar-terrestrial relations – cosmic rays

1. Introduction

The ESA/NASA Solar Orbiter spacecraft (S/C, Müller 2020; García Marirrodriga et al. 2021) hosts six remote sensing and four in situ instruments to image the Sun and to monitor the plasma and the interplanetary magnetic field, respectively. This mission was launched on February 10, 2020 at 4:03 UT from Cape Canaveral (Florida, USA). The S/C cruise period has been characterized by an epoch of minimum-to-low solar activity during the increasing phase of solar cycle 25 and a positive polarity period of the global solar magnetic field (GSMF). The next GSMF polarity change is expected at the maximum of solar cycle 25 between 2024 and 2025 (Singh & Bhargawa 2019). The Solar Orbiter S/C will orbit the Sun between 0.28 AU and 1 AU, with a maximum inclination about the solar equator of 33 degrees during the mission operations.

Metis is the Solar Orbiter coronagraph aimed at imaging the solar corona in visible (VL, in the range 580–640 nm) and ultraviolet light (UV, in a $\simeq 20$ nm band around the 121.6 nm Lyman-α line, Antonucci et al. 2020; Romoli et al. 2021). The

Metis instrument is credited with the first direct imaging of the plasma counterpart of a magnetic switchback in the solar corona (Telloni et al. 2022).

Galactic cosmic rays (GCRs) and solar energetic particles (SEPs) interact in the Solar Orbiter S/C and instrument materials. GCRs consist approximately of 98% of protons and helium nuclei, 1% electrons and 1% nuclei with $Z \geq 3$, where percentages are in particle numbers to the total number (Papini et al. 1996). The GCR flux variations as a function of radial distance from the Sun, as well as of the latitude outside the solar equator, time, and energy are discussed in Grimani et al. (2021).

Solar particles in the same energy range of GCRs (above tens of MeV/n) mainly consist of protons (approximately 99% of the total bulk of SEPs, Reames 2021).

Daily proton and helium data gathered above 450 MeV n^{-1} by the AMS-02 magnetic spectrometer experiment aboard the Space Station were recently published until 2019 (Aguilar et al. 2021, 2022). Unfortunately, these measurements do not overlap the mission operations of Solar Orbiter and therefore GCR model predictions are adopted as input spectra for Monte Carlo simulations (Vlachoudis 2009; Battistoni et al. 2014; Böhlen et al. 2014) aimed at studying the high-energy particle impact on the corona images gathered with both VL and UV detectors as part of the Metis diagnostics.

GCR matrices gathered with the VL instrument in 2022 were visually analyzed for the purposes of carrying out a comparison with a previous work based on 2020 images and Monte Carlo simulations (Grimani et al. 2021). The efficiency of the algorithm for the detection of VL image pixels hit by cosmic rays with respect to those fired by photons is estimated by taking into account the role of both abundant and rare cosmic-ray species.

The increase in spurious pixels fired in the Metis images by solar particles, in addition to GCRs, is discussed here for the first time.

In Sect. 2, we briefly describe the Metis coronagraph. In Sect. 3, we report the energy spectra of galactic nuclei, electrons and positrons for the first part of the Solar Orbiter mission in the summer 2020. The estimates of the proton and helium energy spectra for the year 2022 are also presented. The role of rare GCR particles in 2022 is inferred from the 2020 analysis. In Sect. 4, we report the energy spectra of protons observed during solar energetic particle events of different intensities. In Sect. 5, we discuss the results of a visual analysis of cosmic-ray matrices gathered in 2020 and 2022. Finally, in Sect. 6, the Monte Carlo estimates of the number of pixels fired by abundant and rare cosmic rays in the Metis VL and UV images are compared to cosmic-ray matrix observations gathered with the VL instrument. In addition, the role of SEP events is evaluated.

2. The Metis coronagraph

Metis is the Solar Orbiter coronagraph aimed at carrying out the first simultaneous imaging of the off-limb solar corona in both VL in the range 580–640 nm and UV H I Lyman-α line at 121.6 nm. The instrument and first light images are described in detail in Antonucci et al. (2020), Fineschi et al. (2020), Romoli et al. (2021) and Antonucci et al. (2023).

The Metis design was optimized to achieve a sensitivity to observe the weak corona from 1.7 $R_\odot$ through 9 $R_\odot$ by maintaining a contrast ratio lower than 10^{-9} pointing the Sun center within one arcmin. The VL detector consists of a VL camera with an active silicon CMOS (CMOSIS ISPHI Rev. B developed by CMOSIS Imaging Sensors, now AMS-OSRAM[1], Belgium) sensor segmented in 4.1943×10^6 pixels. Each pixel has dimen-

sions of $10 \, \mu m \times 10 \, \mu m \times 4.5 \, \mu m$ (Antonucci et al. 2020). The geometrical factor of each pixel is 401 μm^2 sr (Sullivan 1971).

The detailed design of the UV detector is illustrated in Uslenghi et al. (2017) and Schühle et al. (2018). It consists of a microchannel plate (MCP) enclosed in vacuum by a magnesium fluoride entrance window 4 mm thick and a fiber-optic output coupler. The MCP has a photocathode coating of potassium bromide (KBr). The UV radiation is converted into electrons that are accelerated against a phosphorus screen. The visible radiation emitted by the screen is captured by a camera system with a STAR1000 image sensor of 1024×1024 pixels (for a total of 1.048576×10^6 pixels) consisting of two units of $15 \, \mu m \times 15 \, \mu m \times 5 \, \mu m$ dimensions. The geometrical factor of each unit is 743 μm^2 sr.

3. Galactic cosmic-ray energy spectra after the Solar Orbiter launch

The comparison of the PAMELA and Ulysses experiments' proton data in the energy range 0.92–1.09 GeV has shown that the GCR intensity changes by +2.7% AU^{-1} with increasing radial distance from the Sun while a negative variation of $0.024 \pm 0.005\%$ degree^{-1} is observed with increasing heliolatitude (De Simone et al. 2011). These findings are in agreement, within errors, with those inferred by Marquardt & Heber (2019), demonstrating that GCRs show radial gradients of $6.6 \pm 4\%$ above 50 MeV and $2 \pm 2.5\%$ in the energy range 250–700 MeV between 0.4 and 1 AU. It can be concluded that GCR flux predictions for Solar Orbiter can be carried out with models optimized with data gathered near Earth.

The Gleeson and Axford model (G&A; Gleeson & Axford 1968) is used to estimate the GCR energy spectra for the Metis diagnostics (see also Telloni et al. 2016; Grimani et al. 2021). This model allows us to predict the cosmic-ray intensity in the inner heliosphere by considering an interstellar energy spectrum and a solar modulation parameter (ϕ) used to account for the energy loss of cosmic rays propagating from the interstellar medium to the point of observations in the inner heliosphere. During GSMF positive polarity epochs, the G&A model has been found to aptly reproduce the GCR measurements at 1 AU in the energy range from tens of MeV to hundreds of GeV (Grimani et al. 2008).

The correlation between the solar modulation parameter[2] and the solar activity is discussed, for instance, in Brehm et al. (2021). The sunspot number, the most widely used proxy for solar activity, is reported in Fig. 1[3] for solar cycle 24 and the first part of solar cycle 25 (see Clette et al. 2014, for details about sunspot number calibration).

It must be stressed[4] that the solar modulation parameter assumes different values for similar conditions of solar activity in case different GCR energy spectra at the interstellar medium are adopted. To this end, we used the solar modulation parameter reported in Usoskin et al. (2011, 2017) estimated with the Burger et al. (2000) interstellar proton spectrum. Unfortunately, no ^{4}He interstellar spectrum is reported in Burger et al. (2000). We choose to use the ^{4}He interstellar spectrum inferred from the balloon-borne BESS experiment data (Shikaze et al. 2007; Abe et al. 2014) that were gathered during different solar modulation and solar polarity periods.

---

[2] See also http://cosmicrays.oulu.fi/phi/Phi_mon.txt
[3] Data used here are publicly available at http://www.sidc.be/silso/datafiles
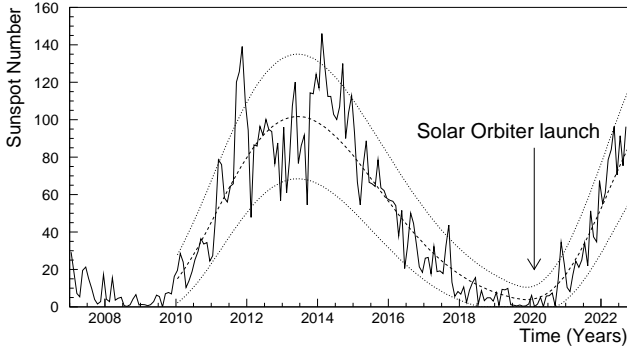[4] http://solarcyclescience.com/solarcycle.html

Fig. 1. Average monthly sunspot number observed since 2006 during solar cycles 24 and 25. Minimum and maximum predictions are indicated by top and bottom dotted lines.

We took the opportunity to verify the reliability of the approach we use for GCR predictions with the LISA Pathfinder mission for which we estimated the charging of the interferometer mirrors in 2016 during solar modulation conditions very similar to those of 2022 (see Grimani et al. 2022, for details). Proton and helium model predictions were compared to monthly averaged observations of the AMS-02 experiment available until 2019. An excellent agreement was found for protons (Aguilar et al. 2021), whereas the model presented a 20% excess for ^{4}He with respect to measurements (Aguilar et al. 2022). The effect of depressing the ^{4}He flux model predictions by 20% on the simulations is discussed in Section 6.

In Fig. 2, we compare our cosmic-ray predictions to proton differential flux measurements gathered in 2020 (solid stars) and in 2022 (solid dots) by the EPD/HET instrument hosted aboard Solar Orbiter. The EPD/HET data are publicly available on the Solar Orbiter Archive (SOAR)[5].

In Grimani et al. (2021), we demonstrate that during conditions of solar modulation similar to those observed in the summer 2020, the minimum and maximum solar modulation parameter was plausibly ranging between $300\,\mathrm{MV\,c^{-1}}$ and $340\,\mathrm{MV\,c^{-1}}$. This upper limit for ϕ was estimated but disregarded because the proton EPD/HET observations were compatible with model predictions obtained by assuming $\phi = 300\,\mathrm{MV\,c^{-1}}$ within model uncertainties and measurements (Wimmer-Schweingruber et al. 2021).

As a matter of fact, the average observed solar modulation parameter in June–July 2020 was $293\,\mathrm{MV\,c^{-1}}$[6]. Therefore, for nuclei, electrons, and positrons, in 2020, we considered the near-Earth energy spectra gathered at solar minimum and reported in Papini et al. (1996), Grimani (2004, 2007), and Grimani et al. (2009).

Nucleus, electron, and positron flux model predictions far from solar minimum and maximum conditions are affected by uncertainties larger than the contribution that these particles give in increasing the number of tracks in the Metis images. The average solar modulation parameter in 2021 was $327\,\mathrm{MV\,c^{-1}}$ and it is plausible to expect for the same not less than $340\,\mathrm{MV\,c^{-1}}$ in June-July 2022. On the basis of these considerations and of the EPD/HET proton data shown in Fig. 2, we adopted the maximum value of the solar modulation parameter set for the Solar Orbiter cruise phase ($\phi = 340\,\mathrm{MV\,c^{-1}}$) for the year 2022.

---

[5] https://soar.esac.esa.int/soar/
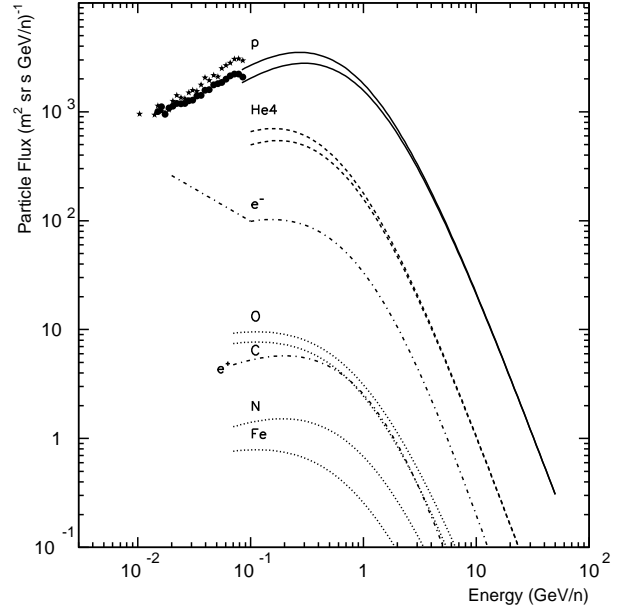[6] http://cosmicrays.oulu.fi/phi/Phi_mon.txt

Fig. 2. Predictions of cosmic-ray energy spectra after the Solar Orbiter launch. The top and bottom continuous (protons) and dashed (^{4}He nuclei) curves are obtained with the G&A model above 70 MeV(/n) for minimum and maximum solar modulation parameter values of $300\,\mathrm{MV\,c^{-1}}$ and $340\,\mathrm{MV\,c^{-1}}$, respectively. Maximum ($\phi = 300\,\mathrm{MV\,c^{-1}}$) and minimum ($\phi = 340\,\mathrm{MV\,c^{-1}}$) proton and helium predictions apply to years 2020 and 2022, respectively. The dot-dashed (dotted) curves indicate the electron and positron (nucleus) energy spectra at solar minimum.

The galactic particle energy spectra above $70\,\mathrm{MeV}$ are parameterized as follows (see for details Armano et al. 2018):

$$F(E) = A\,(E + b)^{-\alpha}\,E^{\beta} \quad \mathrm{particles/(m^2\,sr\,s\,GeV\,n^{-1})}, \tag{1}$$

where E is the particle kinetic energy in GeV/n. The parameters A, b, α, and β for solar minimum in the summer 2020 are reported in Table 1. The units of the parameters A and b are particles/(m^2 sr s (GeV n^{-1})$^{-\alpha+\beta+1}$) and GeV n^{-1}, respectively, while the spectral indices α and β are pure numbers.

A power-law interpolation function was used below $100\,\mathrm{MeV}$ for electron energy spectra, and above $20\,\mathrm{GeV}$ for positrons (Grimani et al. 2009):

$$F(E) = A\,E^{-\beta} \quad \mathrm{particles/(m^2\,sr\,s\,GeV)}. \tag{2}$$

In this last equation, A is measured in particles/(m^2 sr s GeV$^{-\beta+1}$) and β is a pure number.

In Table 1 (from top to bottom), the energy ranges of the parameterizations of the electron flux are: 0.02 GeV–0.1 GeV, and 0.1 GeV–200 GeV. For positrons, they are: 0.07 GeV–20 GeV, and 20 GeV–200 GeV. Proton and helium energy spectra parameterizations for the year 2022 are reported in Table 2. All particle energy spectra are shown in Fig. 2.

As it was mentioned above, due to lack of continuous data gathering in space for electrons, positrons and heavy nuclei, models cannot be tested against observations carried out during intermediate solar activity conditions. Predictions of rare cosmic-ray particle energy spectra were not considered for 2022 due to uncertainties that could potentially be introduced by the model. The contribution of these particles will be estimated in Sect. 6 on the basis of the results obtained at solar minimum.

Table 1. Parameterizations of cosmic-ray energy spectra in June–July 2020.

Particle species	A	b	α	β
p	18 000	0.875	3.66	0.87
He	850	0.53	3.68	0.85
C	23	0.95	3.00	0.32
O	25.2	1.05	3.25	0.32
N	7.0	1.05	3.25	0.5
Fe	1.9	0.95	3.00	0.32
e^- E ≤ 0.1 GeV	24.7			0.60
e^- E > 0.1 GeV	400	0.97	3.66	0.5
e^+ E ≤ 20 GeV	100	1.45	4.1	0.5
e^+ E > 20 GeV	7.61			2.84

Notes. The parameterizations of the energy spectra of protons and nuclei are meant above 70 MeV(/n).

Table 2. Same as Table 1 for protons and helium energy spectra in May 2022.

Particle species	A	b	α	β
p	18 000	0.95	3.66	0.87
He	850	0.58	3.68	0.85

4. Solar energetic particles

The Sun flings one million tons of fully ionized plasma out from the corona every second. The expanding solar wind drags the solar magnetic field forming the interplanetary magnetic field. The typical energy of the solar wind particles is of 0.5–3 keV. Particles of solar origin with energies larger than 1 MeV are observed during "impulsive" and "gradual" events (Reames 2021). Short-duration (≃ hours) impulsive events are generated by magnetic reconnection on open field lines in solar jets, while long-duration (≃ days) gradual events are associated with coronal mass ejections driving shock waves. Pure impulsive or gradual events are rare and shock waves may reaccelerate suprathermal particles from impulsive events. Impulsive and gradual events present different particle energy spectra. Particle acceleration is limited to about 50 MeV during impulsive events. Consequently, due to the average grammage of several g cm^{-2} of S/C and instrument materials stopping low-energy particles before reaching the sensitive parts of the Metis instrument, we estimate the number of pixels fired in the VL and UV images of the solar corona during gradual events only.

It is worthwhile to point out that above tens of MeV, protons overcome by approximately two orders of magnitude the other species of particles during gradual SEP events, as observed in space by the PAMELA magnetic spectrometer experiment that monitored both proton and helium differential fluxes during the evolution of two gradual SEP events dated December 13 and December 14, 2006 (Adriani et al. 2011) up to GeV energies. These two SEP events were characterized by fluences ranging between 10^5 and 10^7 protons cm^{-2} above 70 MeV. The onset of the December 13, 2006 event was observed between 03:18 UT and 03:45 UT, while data were gathered at the peak between 04:33 UT and 04:59 UT. The whole event duration was of two days. The onset of the weak December 14, 2006 event was observed between 23:05 UT on December 14, 2006 and 02:35 UT on December 15, 2006, while the decay phase was measured between 19:30 UT and 23:35 UT of the second day.
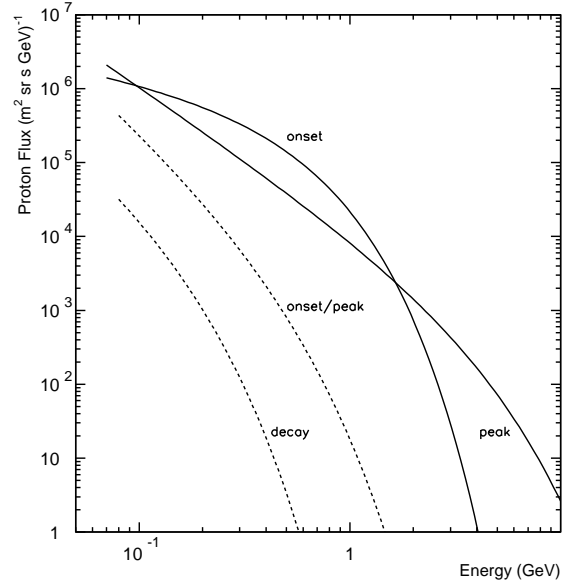

Fig. 3. Solar proton energy spectra measured by the PAMELA experiment during the evolution of the SEP events dated December 13 (solid lines) and December 14 (dashed lines), 2006. The different phases of the events are indicated in the figure.

We focus on these SEP events because data gathered in space with a magnetic spectrometer are certainly the most accurate at high energies to be adopted for Monte Carlo simulations. Unfortunately, most space experiments devoted to solar particle monitoring do not allow for measurements of the particle differential fluxes above 100 MeV(/n). This may most likely be ascribed to evidence that the most frequent solar particle events are characterized by particle acceleration well below hundreds of MeV, even though the major space weather events that lead to substantial S/C inner charging are associated with particles of GeV energies. These SEP events exceed the GCR background by several orders of magnitude. The proton energy spectra observed during the evolution of the December 13 and December 14, 2006 SEP events are shown in Fig. 3 (see also Grimani et al. 2013).

A more recent event characterized by particle acceleration above 2 GeV was observed on October 28, 2021 by several instruments in space, including EPD/HET aboard Solar Orbiter, and with neutron monitors (NMs) on Earth. During this event, Solar Orbiter was almost radially aligned with Earth (see for details Papaioannou et al. 2022; Martucci et al. 2023). The solar eruption started with an X1.0 class flare at 15:17 UT and peaked at 15:35 UT. This event generated the first ground level enhancement for solar cycle 25. The onset of the event was detected aboard Solar Orbiter at 15:35 UT by EPD/HET. Neutron monitor data, binned every 30 minutes, reported the onset at 16:00 UT consistently with the Solar Orbiter measurements. The observed solar proton flux at the onset is represented by the dot-dashed curve in Fig. 4. The contemporaneous availability of the low-energy space data below 100 MeV and observations above 700 MeV gathered on Earth, allowed us to interpolate the two data sets in the 100–700 MeV range.

The most energetic particles are observed at the onset of SEP events, while lower energy particles appear in increasing number at the peak of the event when the high-energy particles fade away (Dalla et al. 2003). In particular, when particle acceleration occurs below 500 MeV, the atmosphere shielding prevents secondary particle production to enhance the NM counting rate, while a large flux of low-energy particles may be associated with
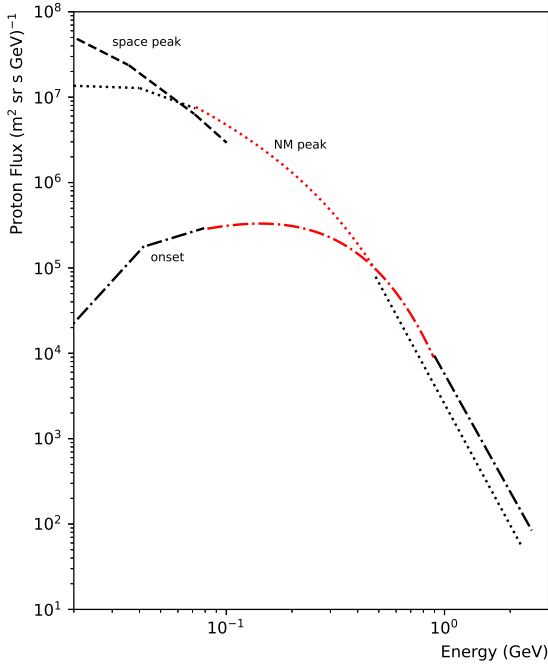
Fig. 4. Solar proton energy spectra observed during the evolution of the solar energetic particle event dated October 28, 2021. The dot-dashed line indicates the onset of the event (15:35–16:35 UT). The dotted line corresponds to the peak of the event observed on ground (17:30–18:20 UT) and the dashed line represents the peak of the event in space (20:35–22:35 UT). Low-energy EPD/HET data below 100 MeV and NM observations above 700 MeV have been interpolated between 100 MeV and 700 MeV according to Grimani et al. (2013, red lines).

the peak of the event in space. As a matter of fact, the October 28, 2021 event peak was observed on Earth at 18:00 UT (dotted curve in Fig. 4), while the peak in space was detected between 20:35 UT and 22:35 UT (dashed curve in Fig. 4). No enhancement of the NM counting rate was observed on Earth at this time. As a result, the peak proton flux in space was not interpolated at energies above the range of availability of the Solar Orbiter/HET data.

Unfortunately, no Metis VL cosmic-ray matrices were acquired during the period of the October 28, 2021 SEP event. On the other hand, the UV images do not allow us to carry out an effective visual analysis of particle tracks due to the high number of spurious fired pixels present in the images resulting very difficult to separate from genuine photon signals. Here, we considered Monte Carlo simulations to estimate the number of pixels fired by solar protons in the Metis images during SEP events as those described above.

5. Visual analysis of VL cosmic-ray matrices in 2022

In Grimani et al. (2021) we have reported the outcomes of a visual analysis of cosmic-ray tracks in four sets of four co-added 15-second cosmic-ray matrices, for a total exposure time of 60 seconds. These images were taken on May 29, 2020.

An algorithm, described in detail in the above work, allows us to separate pixels fired by VL photons from those crossed by high-energy particles depositing a larger amount of energy by ionization in the CMOS of the VL instrument (see also Andretta et al. 2014). An average of 271 ± 22 cosmic-ray tracks per set of images were observed after removing the noisy pix-

els found in more than one image of each set, corresponding to a fraction of about 10^{-5} of the total number of image pixel sample. The noisy pixels were found one order of magnitude smaller with respect to those fired by cosmic rays. The lower limit to the cosmic-ray pixel firing efficiency was estimated equal to 0.94 ± 0.02 by studying a sample of particle slant tracks.

A new analysis of images gathered from May 9 through May 15, 2022 was carried out to test the stability of the instrument performance after two years during the increasing phase of the solar cycle 25. We studied three sets of 14 superposed frames of 30 seconds each comprise a total 7 minute exposure time. The visual analysis was carried out with the APViewer adapted to the new sets of images and described in detail in Grimani et al. (2021).

Noisy single pixels, clusters and columns of fired pixels appearing in more than two images have been removed. The percentage of spurious pixels and the efficiency of single pixels have been found compatible with the first analysis. This evidence indicates that the performance of the VL instrument remained unchanged during the first two years of the Solar Orbiter mission.

Particle straight tracks (single fired pixels) and slant tracks were easily identified. In addition, we found samples of clusters of pixels compatible with a main particle track and side fired pixels. These clusters are displayed as "squares" and "composite tracks" in Fig. 5.

The total number of straight tracks, slant tracks firing more than one pixel, with or without extra pixels fired along the main particle track, are reported in Table 3 after the normalization of data to a 60 second exposure time, meant for a comparison with the first analysis. The average number of particle tracks of 212 ± 6 is observed to be smaller with respect to the 2020 observations. This is expected due to the increasing solar activity during the last two years and the consequent reduction of the GCR flux.

6. Monte Carlo simulations of high-energy particles firing spurious pixels in the Metis VL and UV images

6.1. Galactic cosmic rays

The geometry of the Solar Orbiter S/C and instruments built with Flair (Vlachoudis 2009) in FLUKA (version 4.0.1) for the Metis VL and UV detector simulations is shown in Fig. 6. Details of the VL and UV instruments are shown in the magnified images. The geometry includes the S/C structure, thrusters, fuel tanks and the SPICE, EUI, PHI, and STIX instruments (García Marirrodriga et al. 2021, and references therein). Interplanetary and galactic particles cross from about $1\,\mathrm{g\,cm^{-2}}$ to more than $10\,\mathrm{g\,cm^{-2}}$ of material depending on the particle incidence direction before reaching the Metis VL and UV instruments.

The simulations for the year 2020 returned 276 ± 17 pixels fired by incident protons only in 60 seconds of exposure time. This number of tracks appeared similar to the observations within the statistical uncertainties.

It was suggested that the Metis VL detector could play the role of a proton monitor, in cases where the efficiency of the algorithm for cosmic-ray track removal from VL images was approximately 35% of the proton contribution; that is, numerically equivalent to the sample of particle tracks generated by the other components of GCRs (Grimani et al. 2021). The actual efficiency of the VL instrument algorithm for cosmic-ray
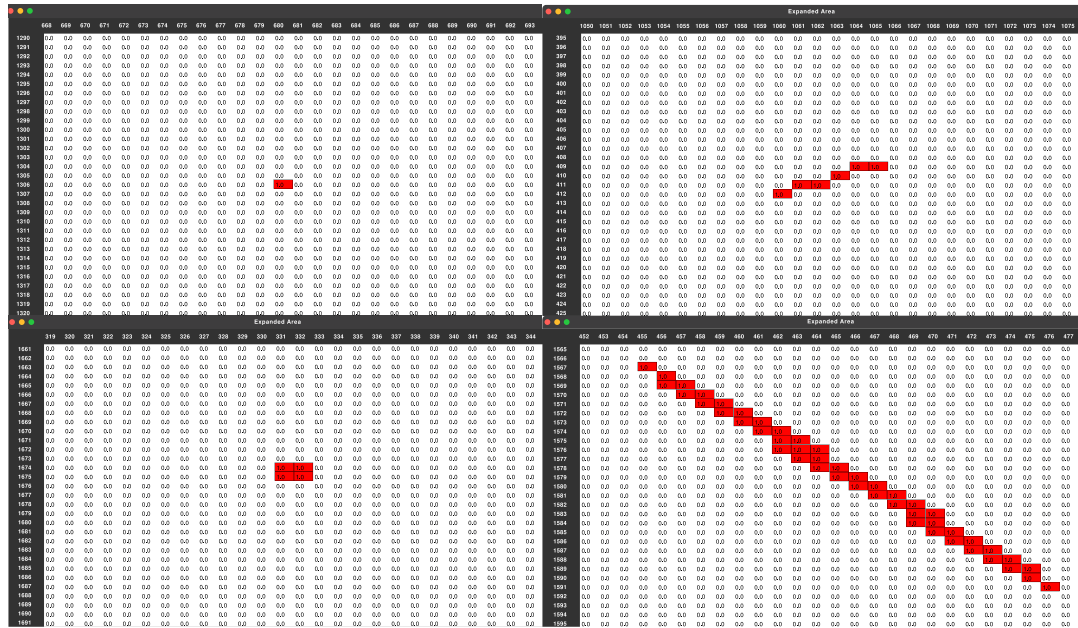
Fig. 5. Particle tracks in the Metis VL cosmic-ray matrices gathered in 2022. Top-left panel represents a single fired pixel associated with straight tracks, while the top-right panel shows a typical slant track. The bottom left and right panels report a square and an exceptional composite track, respectively. Both squares and composite tracks are considered to be formed by pixels in the same line crossed by the incident particle and extra pixels fired by photons and knock-on electrons generated along the main cosmic-ray track. Future works will allow us to verify this hypothesis.

Table 3. Metis cosmic-ray observations in three 7-minute exposure time images gathered in May 2022 by the Metis VL instrument.

	Straight	Slant	Squares	Total	Composite
May 2022					
Image 1	165	60	2	227	19
Image 2	130	63	6	199	23
Image 3	159	49	3	211	19
Average	151	57	4	212 ± 6	20
May 2020					
Average	188	79	4	271 ± 22	23

Notes. Data have been normalized to one minute exposure time for comparison with the first analysis carried out at solar minimum in 2020. Examples of the track topology are reported in Fig. 5.

Fig. 6. Solar Orbiter geometrical model. Remote sensing instruments and electronic boxes are visible. The magnified images show the VL and UV detectors.

detection is estimated here since the solar modulation parameter in the summer 2020 is now known.

The visual analysis of the Metis VL images does not allow us to disentangle primary and secondary particles and the different kinds of particles. As a result, the Monte Carlo simulations play a primary role to study the number of single and clustered pixels fired by high-energy particles in the Metis cosmic-ray matrices.

Rare particle energy spectra are determined at solar minimum according to Papini et al. (1996) and Grimani et al. (2022).

During periods of low solar activity simulation outcomes are affected by two systematic uncertainties of about 10% associated with cosmic-ray models and FLUKA Monte Carlo program accuracy (Lechner et al. 2019).

In the majority of cases, cosmic rays fire single pixels in the Metis images. Observations and simulations return a similar number of slant-to-straight tracks compatible with the isotropic distribution of cosmic rays incident on the Solar Orbiter spacecraft and the geometrical shape of the sensitive parts of the instruments.
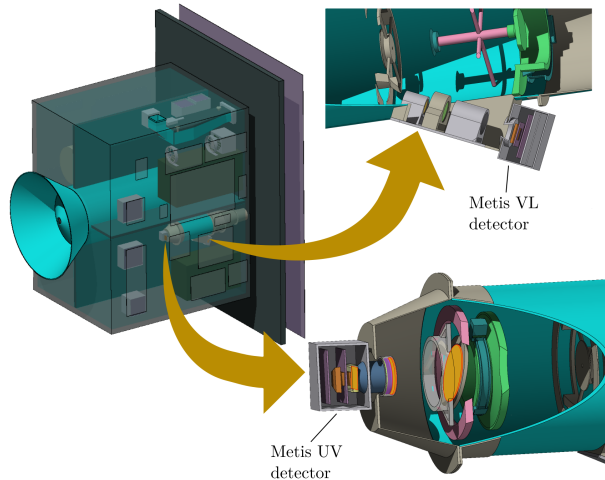
The contributions of nuclei, electrons and positrons to the overall sample of pixels fired by cosmic rays reported in Table 4 actually amount to 38%, thus confirming our prediction of the VL instrument algorithm efficiency for cosmic-ray selection. Simulations reveal also that cosmic rays fire approximately twice the number of pixels in the UV images with respect to those in the VL images mainly because of a larger geometrical factor of the UV instrument, but also because of a different amount of matter surrounding the sensitive parts of the UV and VL cameras. Due to the increasing solar activity over the last two years, in 2022 the proton and helium fluxes are expected to show a decrease of no less than 15% with respect to summer 2020.

The simulated number of spurious pixels fired in the VL images by cosmic-ray protons and helium nuclei decreases by 13% as can be observed in Table 5 (numbers in parentheses

Table 4. Galactic cosmic-ray tracks in the Metis images from Monte Carlo simulations for a 60 second exposure time in the summer 2020.

Particle species	VL detector	UV detector
Protons	276	442
Helium	77	110
Carbon	4	7
Nitrogen	2	3
Oxygen	5	6
Iron	2	2
Electrons	14	24
Positrons	1	1
	$381 \pm 53 \pm 20$	$595 \pm 83 \pm 24$
Total	381 ± 57	595 ± 86

Notes. Systematic, statistical and total uncertainties are indicated and combined in quadrature.

for ^{4}He). With respect to the helium nuclei contribution, Monte Carlo simulations indicate that if a reduction of the input flux of 20% is considered, the contribution of these nuclei to the overall sample of tracks is decreased by 3%. This effect was not considered in the 2020 analysis, but it is taken into account in the 2022 simulations.

An additional plausible contribution of rare particles of 10% of the sample of tracks generated by protons and ^{4}He should be added to these estimates on the basis of the 2020 results and the assumption of a slightly higher solar modulation parameter in 2022 with respect to 2020.

The analysis of the 2022 VL cosmic-ray matrices returns a smaller number of observed tracks with respect to simulations. Systematic and statistical uncertainties on simulation results are reported in Tables 4 and 5. Simulations and observations are in agreement within slightly more than two standard deviations. We will study the role of the actual solar modulation parameter in summer 2022 in future works.

A smaller decrease in the proportion of fired pixels in the UV images (9%) with respect to VL images was found with the simulations. The summer 2020 simulations indicated that for primary protons, the charged particles crossing the VL images in particle numbers to the total number consisted of 80% protons, 17% electrons and positrons, and 3% pions. For the year 2022, protons are estimated to fire 77% (72%) of the total sample of spurious pixels in the VL (UV) images, while 18% (22%) of pixels are hit by electrons and positrons and then 5% (6%) by pions. The ratio of secondary-to-primary particles in the UV images appears 5% larger than in the VL images. At the next solar maximum we will test the capability of the VL instrument to work as a proton monitor in comparison to the UV instrument. This work allows us to study the composition of high-energy particles deep into the Solar Orbiter S/C and may result of interest to other instruments such as EUI and STIX.

6.2. Solar energetic particle events

During gradual SEP events, the overall flux of particles observed in space increases by several orders of magnitude. The majority of these events present a fluence in the range 10^6–10^7 protons cm^{-2} above 30 MeV (Nymmik 1999a,b). The events described in Sect. 4 belong to this range of intensities. In Table 6 we report the number of pixels expected to be fired by solar particles during the evolution of these events. By comparing these results with

Table 5. Same as Table 4 for the year 2022.

Particle species	VL detector	UV detector
Protons	242	402
Helium	58 (67)	88 (101)
Rare particles	30	49
	$330 \pm 46 \pm 18$	$539 \pm 75 \pm 23$
Total	330 ± 49	539 ± 78

Notes. The number of tracks ascribable to ^{4}He nuclei in the parentheses indicate the estimate obtained with the Shikaze et al. (2007) interstellar spectrum before normalization on observed data during a period of similar solar activity.

Table 6. Monte Carlo simulations of solar energetic particle tracks in the Metis corona images for a 60 second exposure time during typical events of different intensity.

SEP event	VL detector	UV detector
December 13, 2006 (onset)	24600	56400
December 13, 2006 (peak)	11600	30800
December 14, 2006 (onset/peak)	1380	1980
December 14, 2006 (decay)	180	201
October 28, 2021 (onset)	12960	28680
October 28, 2021 (NM peak)	9000	13380
October 28, 2021 (HET peak)	38400	60000

those appearing in Table 4, it is possible to notice that during weak-to-medium gradual SEP events, the number of pixels hit by high-energy particles increases by 1–2 orders of magnitude and the fraction of spurious fired pixels to the total number of pixels varies from 10^{-4} to 10^{-2}. Stronger events would further affect the VL and UV instrument observations. These predictions will be verified with VL cosmic-ray matrices gathered in the future during SEP events to assess also the impact of solar particles in the S/C inner charging.

7. Conclusions

High-energy particles interact in the Solar Orbiter S/C, thus limiting the efficiency of on-board instruments. It is found that for 60 seconds of exposure time near solar minimum, the number of pixels crossed by galactic cosmic rays in the VL images of the Metis coronagraph is a fraction of about 10^{-4} of the total number of pixels. Monte Carlo simulations of the VL instrument return a similar number of tracks associated with primary galactic protons. The contribution of cosmic-ray nuclei with charge >1, electrons and positrons accounts approximately for the overall efficiency of the on-board algorithm for high-energy particle detection found of 38%.

Simulations of the number of pixels fired in UV images indicate a larger number of tracks with respect to those present in the VL images. This is mainly due to a larger geometrical factor of the UV instrument and to a different material distribution around the two instruments.

The increase of the solar activity during the year 2022 is expected to have reduced the intensity of the GCR flux by at least 15% with respect to the summer 2020. Monte Carlo simulations show a similar decrease in pixels fired by GCRs in the VL images, while the number of tracks in the UV images decreases

by less than 10%, after being contaminated by a larger number of secondaries.

The number of observed and simulated tracks in the VL images in 2022 appears in agreement within slightly more than two standard deviations. The Metis VL instrument has not modified its performance after the mission launch in terms of an excess of spurious fired pixels with respect to the 2020 analysis. A smaller number of observed tracks with respect to simulations may indicate that an overly small solar modulation parameter has been assumed for the simulations.

The Metis VL images enable the monitoring of long-term GCR proton flux variations and SEP event evolution, when compared to Monte Carlo simulations of the instrument performance. The number of Metis corona image pixels fired by high-energy particles is expected to increase by 1–2 orders of magnitude during the evolution of medium-strong SEP events.

This simulation work, meant for the Metis diagnostics, can be also used to study the Solar Orbiter S/C inner charging during the mission operations and to estimate the role of the impact of particle tracks in the images of other instruments such as EUI and STIX.

References

Abe, K., Fuke, H., Haino, S., et al. 2014, Adv. Space Res., 53, 1426
Adriani, O., Barbarino, G. C., Bazilevskaya, G. A., et al. 2011, ApJ, 742, 102
Aguilar, M., Cavasonza, L. A., Ambrosi, G., et al. 2021, Phys. Rev. Lett., 127, 271102
Aguilar, M., Cavasonza, L. A., Ambrosi, G., et al. 2022, Phys. Rev. Lett., 128, 231102
Andretta, V., Bemporad, A., Focardi, M., et al. 2014, in Software and Cyberinfrastructure for Astronomy III, SPIE Conf. Ser., 9152 , 91522Q
Antonucci, E., Romoli, M., Andretta, V., et al. 2020, A&A, 642, A10
Antonucci, E., Downs, C., Capuano, G. E., et al. 2023, Phys. Plasmas, 30, 022905
Armano, M., Audley, H., Baird, J., et al. 2018, ApJ, 854, 113

Battistoni, G., Boehlen, T., Cerutti, F., et al. 2014, Joint International Conference on Supercomputing in Nuclear Applications + Monte Carlo, 06005
Böhlen, T. T., Cerutti, F., Chin, M. P. W., et al. 2014, Nucl. Data Sheets, 120, 211
Brehm, N., Bayliss, A., Christl, M., et al. 2021, Nat. Geosci., 14, 10
Burger, R. A., Potgieter, M. S., & Heber, B. 2000, J. Geophys. Res. Space Phys., 105, 27447
Clette, F., Svalgaard, L., Vaquero, J. M., & Cliver, E. W. 2014, Space. Sci. Rev., 186, 35
Dalla, S., Balogh, A., Krucker, S., et al. 2003, Geophys. Lett. Res., 30, 8035
De Simone, N., Di Felice, V., Gieseler, J., et al. 2011, Astrophys. Space Sci. Trans., 7, 425
Fineschi, S., Naletto, G., Romoli, M., et al. 2020, Exp. Astron., 49, 239
García Marirrodriga, C., Pacros, A., Strandmoe, S., et al. 2021, A&A, 646, A121
Gleeson, L. J., & Axford, W. I. 1968, ApJ, 154, 1011
Grimani, C. 2004, A&A, 418, 649
Grimani, C. 2007, A&A, 474, 339
Grimani, C., Fabi, M., Finetti, N., & Tombolato, D. 2008, Int. Cosmic Ray Conf., 1, 485
Grimani, C., Fabi, M., Finetti, N., & Tombolato, D. 2009, Class. Quant. Grav., 26, 215004
Grimani, C., Fabi, M., Finetti, N., Laurenza, M., & Storini, M. 2013, J. Phys. Conf. Ser., 409, 012159
Grimani, C., Andretta, V., Chioetto, P., et al. 2021, A&A, 656, A15
Grimani, C., Villani, M., Fabi, M., Cesarini, A., & Sabbatini, F. 2022, A&A, 666, A38
Lechner, A., Auchmann, B., Baer, T., et al. 2019, Phys. Rev. Accel. Beams, 22, 071003
Marquardt, J., & Heber, B. 2019, A&A, 625, A153
Martucci, M., Laurenza, M., Benella, S., et al. 2023, Space Weather, 21, 2022SW003191
Müller, D., St. Cyr, O. C., Zouganelis, I., , et al. 2020, A&A, 642, A1
Nymmik, R. 1999a, in 26th Int. Cosmic Ray Conf. (Salt Lake City), 6, 268
Nymmik, R. 1999b, in 26th Int. Cosmic Ray Conf. (Salt Lake City), 6, 280
Papaioannou, A., Kouloumvakos, A., Mishev, A., et al. 2022, A&A, 660, L5
Papini, P., Grimani, C., & Stephens, S. 1996, Nuovo Cim. C, 19, 367
Reames, D. V. 2021, Solar Energetic Particles. A Modern Primer on UnderstandingSources, Acceleration and Propagation, 978
Romoli, M., Antonucci, E., Andretta, V., et al. 2021, A&A, 656, A32
Schühle, U., Teriaca, L., Aznar Cuadrado, R., et al. 2018, in Space Telescopes and Instrumentation 2018: Ultraviolet to Gamma Ray, eds. J. W. A. den Herder, S. Nikzad, & K. Nakazawa, SPIE Conf. Ser., 10699, 1069934
Shikaze, Y., Haino, S., Abe, K., et al. 2007, Astropart. Phys., 28, 154
Singh, A. K., & Bhargawa, A. 2019, Ap&SS, 364, 12
Sullivan, J. 1971, Nucl. Instrum. Methods, 95, 5
Telloni, D., Fabi, M., Grimani, C., & Antonucci, E. 2016, AIP Conf. Proc., 1720, 100001
Telloni, D., Zank, G. P., Stangalini, M., et al. 2022, ApJ, 936, L25
Uslenghi, M., Schühle, U. H., Teriaca, L., Heerlein, K., & Werner, S. 2017, in Society of Photo-Optical Instrumentation Engineers (SPIE) Conference Series, ed. O. H. Siegmund, SPIE Conf. Ser., 10397, 103971K
Usoskin, I. G., Bazilevskaya, G. A., & Kovaltsov, G. A. 2011, J. Geophys. Res. (Space Phys.), 116, A02104
Usoskin, I. G., Gil, A., Kovaltsov, G. A., Mishev, A. L., & Mikhailov, V. V. 2017, J. Geophys. Res. (Space Phys.), 122, 3875
Vlachoudis, V. 2009, in International Conference on Mathematics, Computational Methods & Reactor Physics (M&C 2009) (New York: Saratoga Springs), 790
Wimmer-Schweingruber, R. F., Pacheco, D., Janitzek, N., et al. 2021, A&A, 656, A22